Pramote Hochareon

Keefe B. Manning

Arnold A. Fontaine

The Pennsylvania State University,
Department of Bioengineering,
University Park, PA 16802

John M. Tarbell
The City College of New York,
Department of Biomedical Engineering,
New York, NY 10031

Steven Deutsch
The Pennsylvania State University,
Department of Bioengineering,
University Park, PA 16802

Wall Shear-Rate Estimation Within the 50cc Penn State Artificial Heart Using Particle Image Velocimetry

Particle image velocimetry (PIV) has been gaining acceptance as a routine tool to evaluate the flow fields associated with fluid mechanical devices. We have developed algorithms to investigate the wall shear-rates within the 50cc Penn State artificial heart using low magnification, conventional particle image velocimetry (PIV). Wall shear has been implicated in clot formation, a major post-implant problem with artificial hearts. To address the issues of wall scattering and incomplete measurement volumes, associated with near wall measurements, we have introduced a zero masking and a fluid centroid shifting technique. Simulations using different velocity fields were conducted with the techniques to assess their viability. Subsequently, the techniques were applied to the experimental data collected. The results indicate that the size of the interrogation region should be chosen to be as small as possible to maximize resolution while large enough to ensure an adequate number of particles per region. In the current study, a 16×16 interrogation window performed well with good spatial resolution and particle density for the estimation of wall shear rate. The techniques developed with PIV allow wall shear-rate estimates to be obtained from a large number of sites at one time. Because a planar image of a flow field can be determined relatively rapidly, PIV may prove useful in any preliminary design procedure. [DOI: 10.1115/1.1784477]

Introduction

A major cause of artificial heart failure after implantation is clot formation [1–3] The primary connection between the chamber flow field and the complex clotting process is still unknown, although the wall shear stress is a primary suspect. Many studies have been performed to investigate the relationship of wall shear stress on in vivo clot formation [4–6]. In the following, we concentrate on studies performed in artificial hearts.

Particle streak flow visualization, using amberlite resin particles, was performed to photograph the flow patterns within an artificial heart [7–8]. The qualitatively low and high velocity regions were used to predict regions of stagnation or high wall stress. Affeld et al. [9] reported dye-washout techniques that were used to detect regions of high shear or stagnation. The areas of low dye removal corresponded with regions associated with thrombi formation. Tarbell et al. [10] used pulsed Doppler ultrasound to estimate the local wall shear stress at 12 positions around the periphery of a flexible blood sac of an artificial heart. The wall shear stress was calculated by measuring the near wall velocity approximately 1 mm away from the wall and computing the near wall gradient. The peak wall shear stress was approximately 25 dynes/cm^2. Phillips et al. [11] used laser Doppler anemometry (LDA) to measure the near wall gradient, with the closest measured velocity 0.5 mm from the wall. Measurements were obtained at three locations suspected of flow separation, recirculation, and stasis. Estimated wall shear stresses ranged from 1.8–53 dynes/cm^2.

Wall shear-rate measurements using flush-mounted hot-film anemometry were done by Baldwin et al. [12–13]. Peak wall shear stresses were measured at 2700 dynes/cm^2 and 1400 dynes/cm^2 near the aortic and mitral valves, respectively. However, these results were dependent on the orientation of the hot-film relative to the flow direction. Flow within the artificial heart chamber is complex, and unsteady; thus, the direction of flow could vary significantly during each pump cycle. Because of this three-dimensionality, the wall shear stresses obtained from the hot-film technique could not be obtained with high accuracy. The technique requires both modification to the test model and calibration outside the model. It is not practical to obtain good spatial definition of the wall shear stress using multiple flush-mounted hot-film. Moreover, as a heat transfer device, the hot-film technique cannot measure low wall shear-rates with any accuracy. Laser Doppler anemometry measurements within the 70cc Penn State Artificial Heart have revealed areas of three dimensional flow fields including turbulent flows especially in the region of the mechanical heart valves [14]. The Reynolds stresses in the regurgitant jets that develop after valve closure have been measured at up to 20,000 dynes/cm^2 on the minor orifice sides of the aortic and mitral valves. A vortex or recirculating flow pattern develops within the heart chamber during diastole, which provides washout along the chamber walls.

Our approach here is to use particle image velocimetry (PIV); a technique widely used in fluid experiments for over a decade. Particle image velocimetry utilizes the concept of particle displacement over a specified small finite separation time to compute the velocity vector field. The technique allows a noninvasive experimental arrangement and provides a quantitative, instantaneous velocity vector field with comparable spatial resolution to that obtained by LDA. A well-populated particle velocity field is the attraction of PIV to fluid dynamic studies and distinguishes PIV from other flow measurements, as it allows for instantaneous velocity gradient computation. Particle image velocimetry has been used almost exclusively to measure velocities, although work by Kertzscher et al. [15] to identify wall shear rates, making use of a thin light sheet near the wall, has recently appeared. Raffel et al. [16] has published a complete review of PIV: the concept, methodology, data processing and post processing analysis. A detailed

---

Contributed by the Bioengineering Division for publication in the JOURNAL OF BIOMECHANICAL ENGINEERING. Manuscript received by the Bioengineering Division July 28, 2003; revision received January 21, 2004. Associate Editor: A. Yoganathan.

theoretical background of PIV can be found in the work of Keane and Adrian [17–18]. For completeness, we include a brief discussion of the technique.

Particle Image Velocimetry

Particle image velocimetry measures the particle displacement over a specified small finite separation time, ΔT. For planar PIV, as used here and by most conventional systems, a thin light sheet is used to illuminate the particles, and the velocity vectors are computed by $u = \Delta x/\Delta T$ and $v = \Delta y/\Delta T$. Therefore, the main direction of particle displacement should be aligned with the light plane. Two images of the flow field are recorded at times T and $T+\Delta T$. The technique requires that the fluid must contain an adequate number of small particles to permit accurate cross-correlation statistics and that the presence of the particles in the flow do not significantly disturb the original flow characteristics. Crowe et al. [19] determined that these suspended particles faithfully follow the surrounding mean flow provided that the particle relaxation time, τ_s, estimated using a Stokes flow analysis as: $\tau_s = d_p^2 \rho_p / 18\mu$ is much smaller than ΔT. Crowe et al. indicates that for negligible particle-fluid velocity differences the Stokes number, $St_{PIV} = \tau_s / \Delta T$, always less than 0.02 here, must be much less than 1. In practice, τ_s is made small by using very small particles. As to the number of particles required, Monte Carlo simulations have indicated $N_I > 5$ is needed to obtain a 95% valid detection probability in cross-correlation of a double frame/single exposure [16,18].

Digital PIV calculates a 2D cross-correlation on small subregions, called ‘‘interrogation windows,’’ within a PIV image to obtain an average particle displacement within that interrogation region. The cross-correlation function works as pattern recognition of the particle distribution between the first and second frames. The cross-correlation peak occurs where the second frame of the interrogation window is shifted by the group particle displacement. Therefore, the displacement gradient of each particle must be small enough that the pattern is minimally distorted over the separation time. The displacement gradient is the gradient of the particle displacement as a function of distance from the wall ($d(\Delta x)/dx$ and $d(\Delta y)/dy$). The particle distribution pattern can also be distorted by particle loss between the first and second frames of an interrogation window. In-plane particle loss means that the particles in the first frame move out of the interrogation window in the second frame, but are still in the light plane; while out-of-plane particle loss means the particles in the first frame leave the light plane.

High velocity gradients can also result in a distorted particle distribution pattern. Distorted particle distribution patterns on the cross-correlation function can manifest as a low signal to noise ratio, or as multiple peaks, either of which reduces the accuracy of the resulting displacement vector.

The size of the interrogation window and the time separation can be varied to minimize the distortion and increase the accuracy of the cross-correlation. Larger interrogation windows usually reduce the in-plane particle loss, but at a cost of an increased gradient within the interrogation window. Since the interrogation window's size determines the spatial resolution of the measured displacement vectors, smaller windows are more favorable in practice as long as good accuracy is obtainable. Second window offsetting schemes, such as iterative and multigrid methods [20–21] are often used to reduce bias from in-plane particle loss. Reducing the separation time helps minimize the out-of-plane particle loss and also reduces the displacement gradient. ‘‘High gradient correction’’ [22] or ‘‘cross-correlation based correction’’ [23] algorithms are used to minimize the error due to multiple peaks (cross-correlation function). The recorded images in digital PIV are recorded into 8-bit to 12-bit gray scale that is capable of providing a displacement accuracy of one tenth to one twentieth of a pixel [16]. Too small a particle displacement (smaller than one tenth of a pixel) may not be resolved by the standard cross-correlation algorithm.

Extension of the standard PIV technique to near wall strain rate estimates presents challenges that must be resolved for accurate wall shear approximations. In cases where the boundary layer on the wall remains attached, the focus of this study, the gradient at the wall is usually higher than that in the flow region. Particle image velocimetry assumes the particle image distribution near the wall is homogenous. For a near wall measurement, a particle-free-region close to the wall [24] should not be observable in the images, the image distortion caused by the wall curvature should be minimal, and the wall vibration and wall location uncertainty should be negligible. In this study, the practical interrogation window size could be reduced to 16×16 pixels with reasonably accurate results (adequate particle density, minimal wall distortion) for a given resolution and magnification. As the magnification increases, the conditions described above break down, and conventional PIV may not provide accurate results. Increased image magnification while maintaining good image quality is the appropriate means of solving the high velocity gradient problem [17,25–26] in PIV processing.

Higher image magnification does add constraints on maintaining adequate particle density per interrogation region. This constraint becomes problematic along a solid surface. In particle laden shear flow on a solid surface, particles migrate from the near wall region due to the velocity gradient on the wall. This will generate a near particle free region along the wall covering a small finite distance from a surface and presents challenges for PIV image processing at a wall where it is difficult to maintain an adequate local particle density. The size of this zone is a function of several parameters, the particle size, magnitude of the velocity gradient, presence of turbulence, secondary flow features, buoyancy and wall curvature to name a few. This particle free zone becomes a problem in PIV when the size of the interrogation region approaches the size of the particle free region to within an order of magnitude. This can occur with very small interrogation regions in normal magnification or for most interrogation regions at high magnification. The impact of this particle free zone would be to 1) increase noise in the velocity estimate, 2) inhibit estimation of a valid displacement resulting in no velocity estimate for that region, or 3) a velocity estimate that is biased high relative to the spatial location the PIV algorithm assigns to it. This biased estimate can result from having a sufficient number of particles in the interrogation region for a valid displacement estimate, but where the location of these particles is shifted away from the wall. Since the PIV algorithm will assign the location of the center of the interrogation region as the location of the velocity vector, the vector will be displaced slightly from the region the particles used to estimate it were from.

The authors took care to make sure that the size of the minimum interrogation region was large enough to contain at least 5 particles per image at these normal magnifications. Other benefits of the relatively low magnification PIV used here are: (i) a larger field of view—providing a general idea of the flow in a larger region, (ii) less experimental and computational effort, and (iii) more flexibility with different types of flows and boundary geometries.

Strong three-dimensionality produces velocity bias through a perspective projection error. Perspective projection is the error due to the particle moving through the light sheet thickness. The projected particle displacement, on the ‘‘image plane’’ may not be the same as the spatial component of the displacement in the ‘‘light plane’’ [16]. The motion across the light sheet in highly 3-D flow can bias the local velocity estimation due to perspective projection, if the particle has not left the light sheet. The effect of perspective projection velocity bias is illustrated in Fig. 1 and is usually more severe at the edge of the observation field, where the projection angle increases. The simulation of 3-D hurricanes from

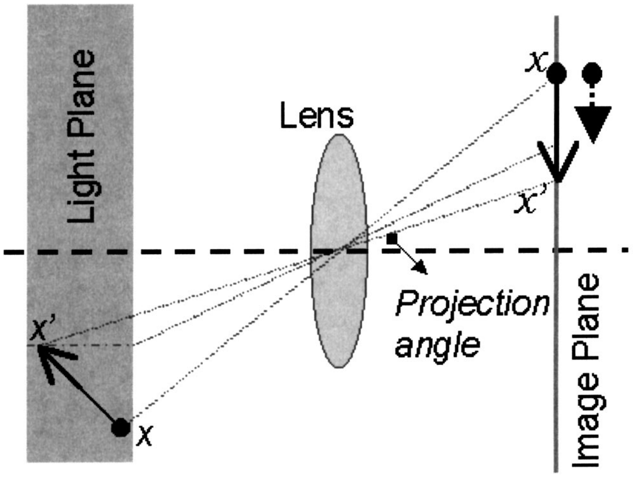

Fig. 1 Illustration of the perspective projection, the dark arrow on the image plane is the vector obtained from perspective projection, the dashed arrow (to the right of the image plane) is the correct projection of the displacement vector on the XY plane.

a non-specified source showed up to 16% velocity error [16]. At high image magnification, the focal length becomes shorter and the projection angle increases, which worsens the perspective projection. Strong perspective projection could vary the magnification factor through the image plane resulting in an image distortion. Three-dimensionality and small-scale flow patterns frequently occur in high gradient regions. Reducing dT minimizes the out-of-plane particle loss, but not the perspective projection error.

Processing of the near wall regions can also introduce bias errors due to the overlapping of interrogation windows with the wall. In PIV, we assume that an interrogation window completely surrounds a fluid volume. The cross-correlated vector is recognized as the average displacement of all the particles within the interrogation volume, and the location of the vector is taken at the center of the interrogation volume. However, this assumption is not valid for an interrogation volume overlying a wall, as the fluid volume only occupies a part of the interrogation volume. This problem can bias both the velocity value and its location. We will introduce two algorithms: a zero masking and a fluid centroid shift to resolve this problem.

In order to calculate velocity gradients from velocity fields obtained by PIV, different numerical differencing schemes, such as central differencing, Richardson extrapolation, and least squares methods have been used [16,27,28]. All of these techniques require neighboring velocity values, which are not available when considering the point closest to the wall. In this case, one-sided interpolation, such as forward or backward differencing needs to be considered. The grid spacing used in these techniques is, moreover, also likely to be non-uniform (or even nonstructured), which further complicates the problem. In addition, the wall location is a critical factor. In this study, the wall location was determined from the images in conjunction with the known wall geometry [29].

The goal in this study is to develop the tools needed to provide accurate mean wall shear-rate estimates from low magnification, conventional PIV images, and to apply these tools to the artificial heart flow field. Although PIV has been applied to investigate turbulent flow fields in a number of applications with excellent results [30–32], the mean flow is the emphasis here. As in LDA, a sufficient number of realizations must be taken for the results to converge. Convergence studies on PIV data obtained using the artificial heart indicated that 200 image pairs were adequate for resolving mean flow statistics.

Methods

A Algorithms. Cross-correlation of acquired images was performed by the TSI Insight 5 software. A recursive or multigrid cross-correlation scheme was used with an initial interrogation window of 64×64 pixels, stepped down by a factor of two to reach the final interrogation windows of 32×32 and 16×16 pixels (two final interrogation sizes were tested to study the effect of the interrogation window). The Hart correlation, a cross-correlation based correction algorithm with sparse array compressed image correlation [33–35], was selected with a bilinear peak finding algorithm. Each interrogation window has 50% overlapping with its neighbors. A range and local median validation criteria [36] were used sequentially for each vector file obtained by Insight 5.

After data validation, the proportion of the number of invalid values to the total number of values for each instantaneous vector field (one vector file) was used to determine the validity of the instantaneous vector field. In this experiment, that tolerance was set to 80%. For the remaining valid vector files, no interpolation and smoothing algorithm was applied to avoid error propagation from neighboring vectors. Averaging was performed vector-by-vector to obtain the ensemble mean velocity field.

Zero masking and a centroid shift technique were developed to address the incompleteness of the interrogation area at the wall, which can add error to the velocity magnitude and location. A velocity bias can result from wall scattering outside the fluid volume that is captured in the interrogation windows. Such scattering is caused by occlusions in the clear acrylic model. Figure 2(*a*) illustrates how the wall scattering, which is ideally dark, can instead have a particle-like pattern. The intensities of the wall scattering are indistinguishable from the particle images. As a result, the cross-correlation recognizes the non-particle scatterings as stationary objects, causing velocity bias toward lower values. The concept for the zero-masking technique is, therefore, to eliminate the non-particle intensity by simply masking the non-fluid area with zero intensity or mean background intensity. The raw image after zero masking is shown in Fig. 2(*b*).

The location of the wall must be known prior to applying the zero-masking technique. The wall location is determined here by manually identifying the pixel coordinates for several reference points along the wall in a randomly selected group of images (roughly 20). These identified reference locations are then used in combination with the known model geometry to mathematically reconstruct the pixel coordinates of the model wall in the image.

Since the interrogation volume is only partly occupied by fluid volume, the appropriate vector location should be the centroid of the actual fluid volume within the interrogation region. Figure 3 illustrates shifting the vector location from the center of the interrogation window to the fluid centroid within the same interrogation window. The dotted arrow at the center of the hatched region in Fig. 3 illustrates shifting the vector location from the center of the interrogation volume to the fluid centroid. The centroid of the fluid region is determined using standard image processing techniques within Matlab. The fluid region is geometrically redefined into sub-pixel resolution by subtracting the known wall location from the pre-defined rectangular interrogation zone. The centroid of this new region is then computed using a center of mass computation.

The zero-masking technique has a minimal processing time impact on the velocity vector calculation. The centroid shifting is used in the estimation of wall shear. The total processing time, in Matlab, performing the centroid shift and the wall shear calculation is less than 1 second per image.

Wall shear-rates are computed from the velocity vectors within a specified distance from the wall—shown as the points with velocity arrows in Fig. 3. Note that, for the points very close to the wall, the interrogation windows may have too small a fluid volume to obtain a valid cross-correlation; therefore, the velocity vectors may not be obtained on those windows. After the velocity

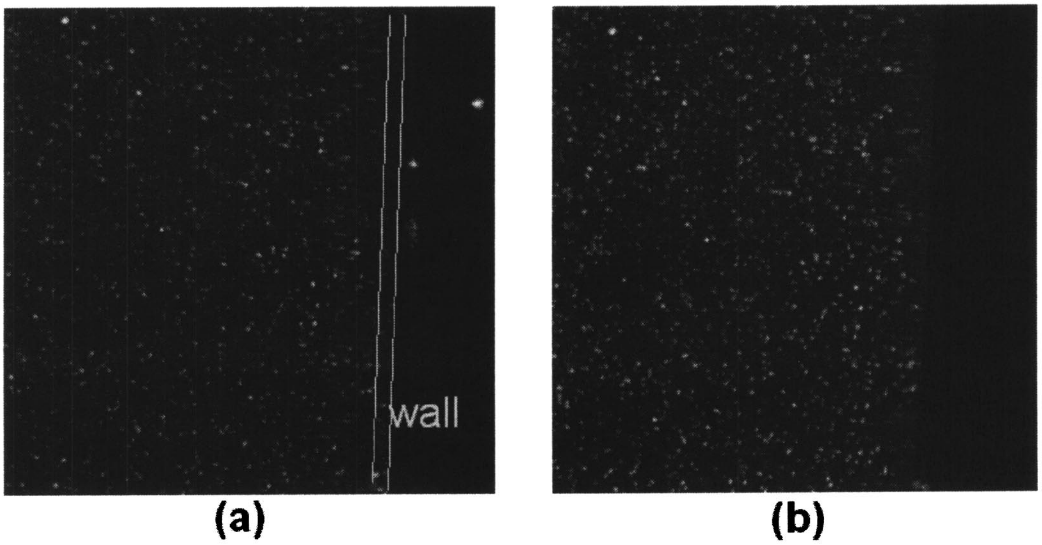

Fig. 2 PIV image (*a*) before and (*b*) after zero-masking.

vectors and their corrected locations are obtained, the vectors are decomposed into local wall coordinates as illustrated in Fig. 4. The wall shear-rate is calculated from the tangential component divided by the normal distance between the vector and the wall. The wall shear-rates obtained by this technique are first order accurate.

The processing algorithm does a good job in providing accurate wall shear-rate estimates. However, the estimates are susceptible to spurious noise due to inaccurate wall displacements. A "segmented local velocity histogram filter" is applied to the resulting wall shear-rate estimates to eliminate spurious shear-rates. Application of this filter involves dividing the entire vector field into small 2-D spatial segments that are larger than the interrogation window. Within the segment, the uniformity of the velocity is assumed, and as a consequence, spatial resolution is unchanged. The histogram filter works by truncating velocity vectors that are out of the accepted range based on the average of vectors in that segment (for example, the first and last 3% might be removed). The remaining vectors within the segment are averaged, and this average is assigned to the center of the segment. The details of the segmented local velocity histogram filter and averaging are described more completely by Hochareon [29].

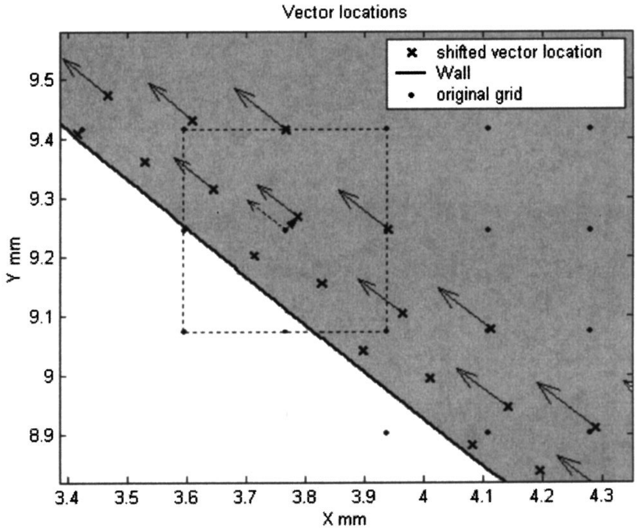

Fig. 3 The illustration of the fluid centroid shift: the gray area represents the fluid region, the dashed square indicates the interrogation window for the vector at the center of the window, and the dashed arrow in each dashed box shows the vector location being shifted to the centroid of the fluid part of the interrogation window.

These algorithms were first tested using simulated PIV data. Artificial PIV images were constructed to simulate velocity fields. A Monte Carlo simulation was used for image reconstruction with ideal image conditions. The particles were evenly and randomly distributed to achieve a minimum of 4 particles per interrogation window. Out-of-plane particle loss was set to 10%, and the particle image intensity was varied in the range of $\pm 20\%$. Four velocity fields were used for the simulations: a linear and a quadratic profile on both a straight and a curved surface and are illustrated in Fig. 5.

The displacement at the wall was also varied linearly along the streamwise direction. Each velocity field was reconstructed for 80 image pairs and was processed with and without zero masking. Therefore, the effects of profile type, wall curvature, wall dis-

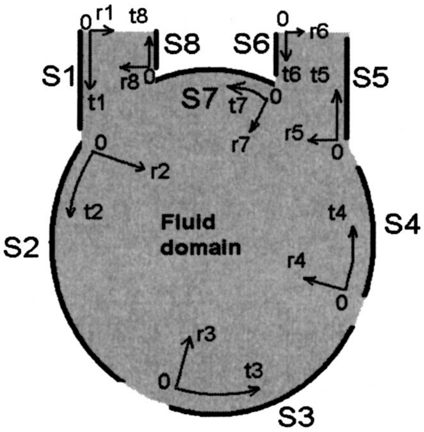

Fig. 4 Wall coordinate systems: S—surface, r—normal axis pointing into the fluid domain, t—tangential axis pointing in counter-clockwise direction, and O—origins. The imaged plane is 5 mm from the frontal edge.

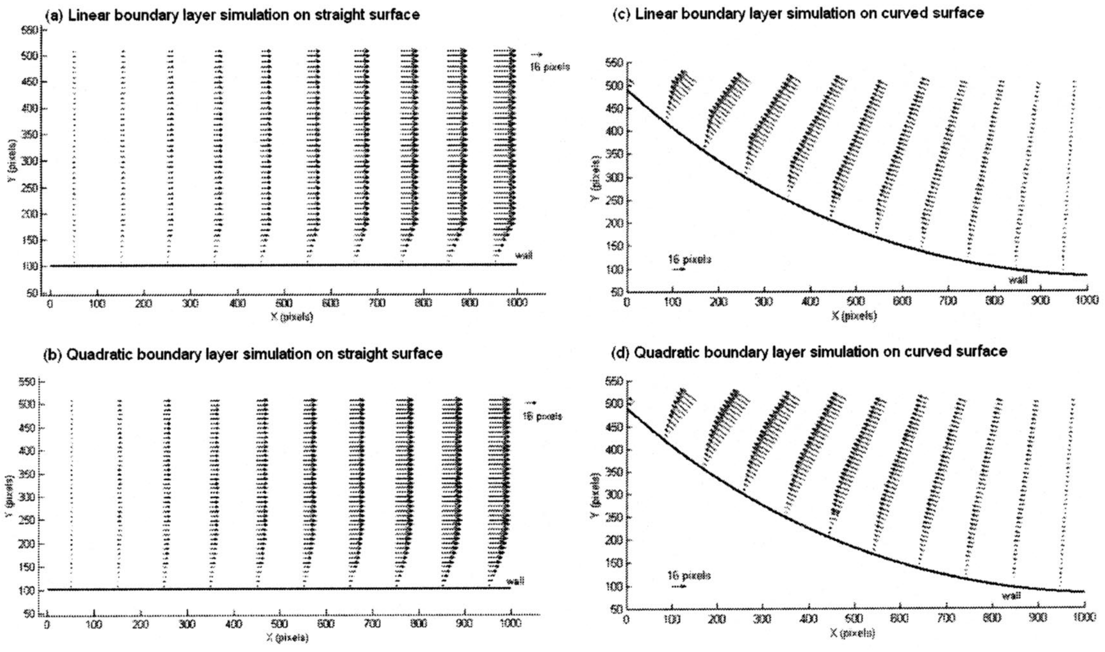

Fig. 5 Four velocity fields used for the simulations: (*a*) a linear profile on a straight surface, (*b*) a quadratic profile on a straight surface, (*c*) a linear profile on a curved surface, and (*d*) a quadratic profile on a curved surface.

placement, and wall scattering on the wall shear-rate estimation, as a function of two different interrogation window sizes (32 ×32 and 16×16), were studied in these simulations. The developed algorithms were then applied to the experimental data obtained in the artificial heart model.

B Experimental Setup. A clear Plexiglas model of the 50cc Penn State artificial heart was installed in the Penn State mock circulatory loop [37]. The blood analog fluid was mineral oil (Penreco Inc., Houston, TX), with a specific gravity of 0.827 kg/m^3, a refractive index of 1.46, and a viscosity of 4.7 cP. The geometry of the 50cc chamber is a small scale model similar to the 70cc model used in Baldwin et al. [14]. The operating conditions were on average 5 L/min flow rate, 75 beat/min, and 30/0 and 120/80 mmHg inlet and outlet pressures, respectively.

A dual pulsed Nd:YAG laser (New Wave Research Inc., Fremont, CA) and appropriate cylindrical lens were used to form an approximate 1.5 mm thick light sheet for visualizing the particles. Red fluorescent 7 μm polystyrene particles (Duke Scientific Corp., Palo Alto, CA), with a specific gravity of 1.055 kg/m^3, and approximate excitation/emission wavelengths of 542/612 nm, were used. The Stokes number for this system was less than 0.02 and, thus, the particles were expected to follow the flow. Two hundred PIV image pairs were recorded by a 1024×1018 CCD camera (TSI, Inc., St. Paul, MN) for each location.

Measurement planes are presented from two locations (Fig. 4): the lateral wall of the inlet area (S5), and the bottom wall of the main chamber (S3). Location S5 is a straight surface, while S3 is a curved surface. For all measurements, flow remained attached to these surfaces (200 ms and 300 ms after onset of filling, respectively). The magnification was adjusted to provide pixel resolutions of 24.9 and 21.4 μm/pixel for S5 and S3, respectively. The resulting velocity spatial and the wall shear-rate resolutions with the 32×32 and 16×16 interrogation window sizes were approximately 720 and 360 μm for both measurement locations.

Results and Discussion

A Simulations. Results of the wall shear-rate calculations for four simulations (linear profile on a straight surface, linear profile on a curved surface, quadratic profile on a straight surface, and quadratic profile on a curved surface) were obtained. The results shown in Fig. 6, the linear profile on the straight surface, is representative of each of the simulations. The solid straight line represents the known theoretical profile. Figure 6 shows the shear-

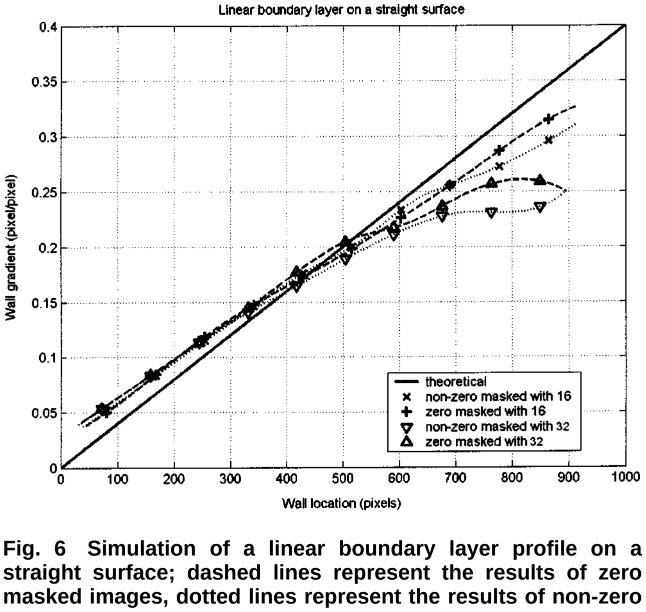

Fig. 6 Simulation of a linear boundary layer profile on a straight surface; dashed lines represent the results of zero masked images, dotted lines represent the results of non-zero masked images, and the numbers indicate the interrogation window size.

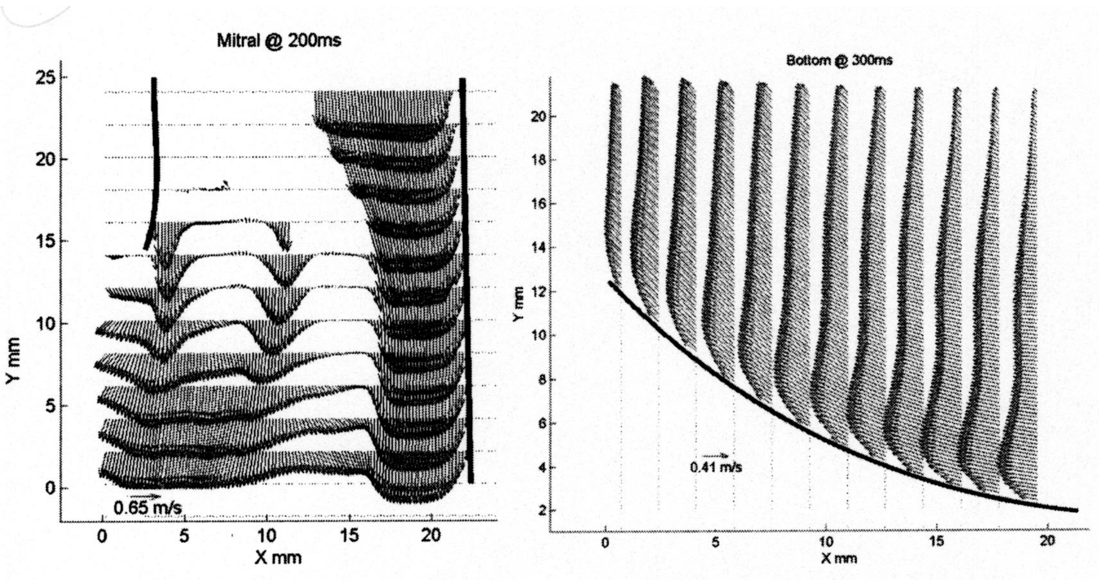

Fig. 7 The average velocity maps from the two measurement locations within the artificial heart chamber: (left) mitral view at 200 ms, (right) bottom view at 300 ms after the onset of filling.

rate profiles of non-zero masked images vs. zero-masked images for different size interrogation windows. The following discussion will address: interrogation window size, wall scattering, and wall gradient. Details of the effect of wall curvature and profile can be found in Hochareon [29].

The results show an error of less than 20% for each interrogation window for low wall displacement gradients in all the simulations with and without zero masking. These displacement gradients are representative of strain rates in the artificial heart. The 16×16 interrogation window performs better than 32×32. Wall scattering does not significantly affect wall shear-rate in this application. We have seen significant effect of wall scattering in our experiments with high magnification imaging (4.2 μm/pixel)—decreasing near wall velocity magnitudes by as much as four times [38]. The particle image quality and density, background intensity, and wall intensity pattern, which vary from the current images and the high-magnification images, may alter the effect of wall scattering on the cross-correlation of the wall interrogation windows.

The large and small interrogation window sizes affect the accuracy of the wall shear estimation. The effect of the high gradient is stronger with large interrogation windows (32×32 pixels). This is not a surprise: larger interrogation windows with high gradients tend to yield cross-correlation functions with multiple peaks. This suggests that 8×8 interrogation windows would be better still, but one must guarantee an adequate number of particles in a smaller interrogation window.

Since standard PIV cross-correlation can resolve only one tenth or one twentieth of a pixel, the smallest displacement should not be smaller. This constrains the lower limit for the particle displacement. With a first order (linear) wall shear-rate calculation, we consider only the vector nearest the wall that is within the interrogation window size (i.e., 16 or 32). The displacement of one tenth of a pixel at the furthest particle location to be cross-correlated gives the lowest (sub-pixel) accurate wall displacement (i.e., 0.00625 and 0.003125). These numbers also represent the resolution of the wall shear-rate estimation. In the situation where increasing ΔT to avoid too small wall displacement gradients is not an option, reducing the wall displacement gradient resolution by increasing the wall shear region may be considered. We have not investigated the exact upper limit of wall displacement gradient since a wall displacement gradient of 0.4 is already high and barely achievable in our experiments due to the out-of-plane particle loss. However, we have learned from this study, that within a 0.4 wall displacement gradient, we can obtain reasonable wall shear rate estimates.

B Experiments. The velocity fields at both measurement locations from the artificial heart experiment are shown in Fig. 7. The resulting wall shear-rates on both surfaces are presented in similar format to that of the simulation results. All the experimental images were zero-masked. Each plot has datasets from two different interrogation window sizes.

The experimental results from the lateral wall are shown in Fig. 8. Both interrogation windows yield similar wall shear profiles of a comparable magnitude. The shear-rate profile is consistent with the boundary layer distribution on the lateral wall of the mitral view of Fig. 7. That is, the larger near-wall velocities occur at the middle portion of the wall. Although 16×16 and 32×32 interrogation windows show quite similar results for moderate shear-rates ($\sim 1000\ \mathrm{s}^{-1}$), the 16×16 window shows much higher peak shear-rates in the large velocity gradient region. We do expect higher wall shear-rates for this attached boundary layer flow, as the resolution increases. This discrepancy may suggest the necessity of higher magnification. Hochareon [29] found high magnification images of the same order of magnitude of the wall shear-rate on the lateral wall, but with a higher peak of approximately $2000\ \mathrm{s}^{-1}$.

Figure 9 shows the resulting wall shear-rate profiles on the bottom wall. Here the shear-rates are more moderate then on the lateral wall and the 16×16 and 32×32 interrogation windows give similar results.

Conclusions

Both simulations and experiments have demonstrated the capability of PIV in providing reasonable wall shear-rate estimates. The simulation suggests that the 16×16 interrogation windows perform well with different flow profiles and geometries. The experimental results confirm the use of the 16×16 interrogation windows for wall shear-rate estimation. The measurement from the lateral wall also demonstrates that the technique is capable of indicating low shear areas.

Investigations of the accuracy of wall shear-rate estimation by PIV have not appeared in the literature. Most PIV work has focused on increasing the accuracy of the velocity vector. Here, to

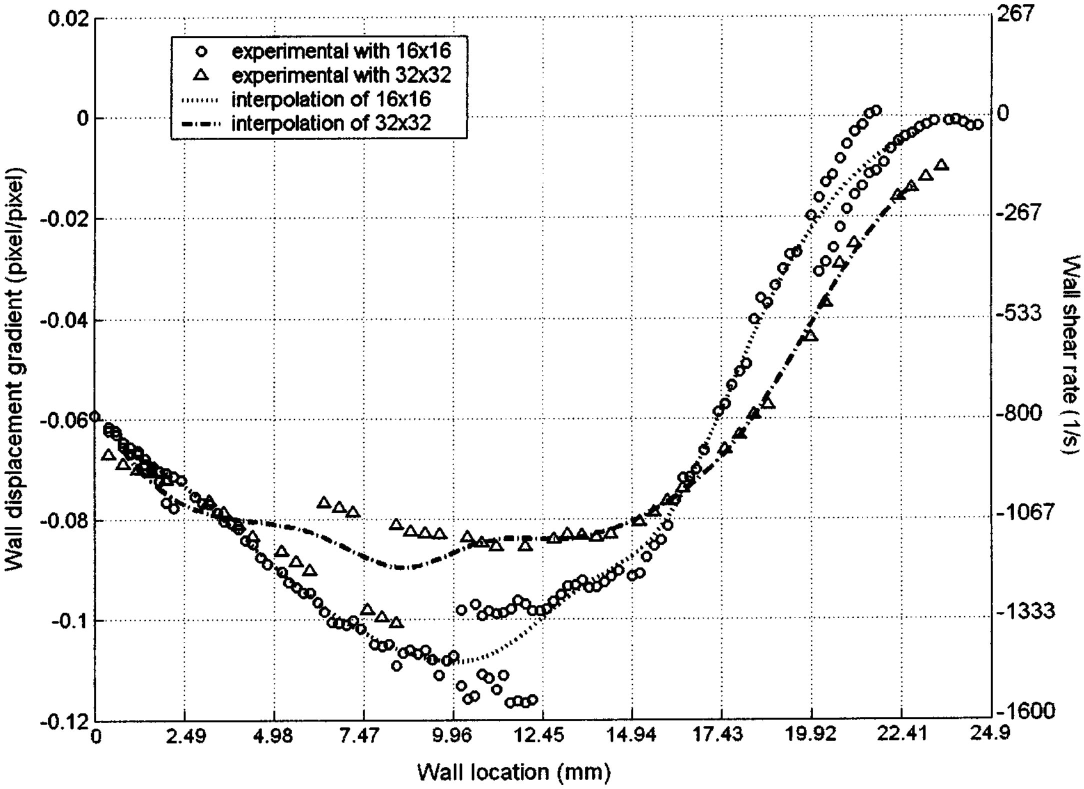

Fig. 8 The wall displacement and wall shear-rate of the lateral wall (straight surface) of the mitral port obtained by two different interrogation window sizes.

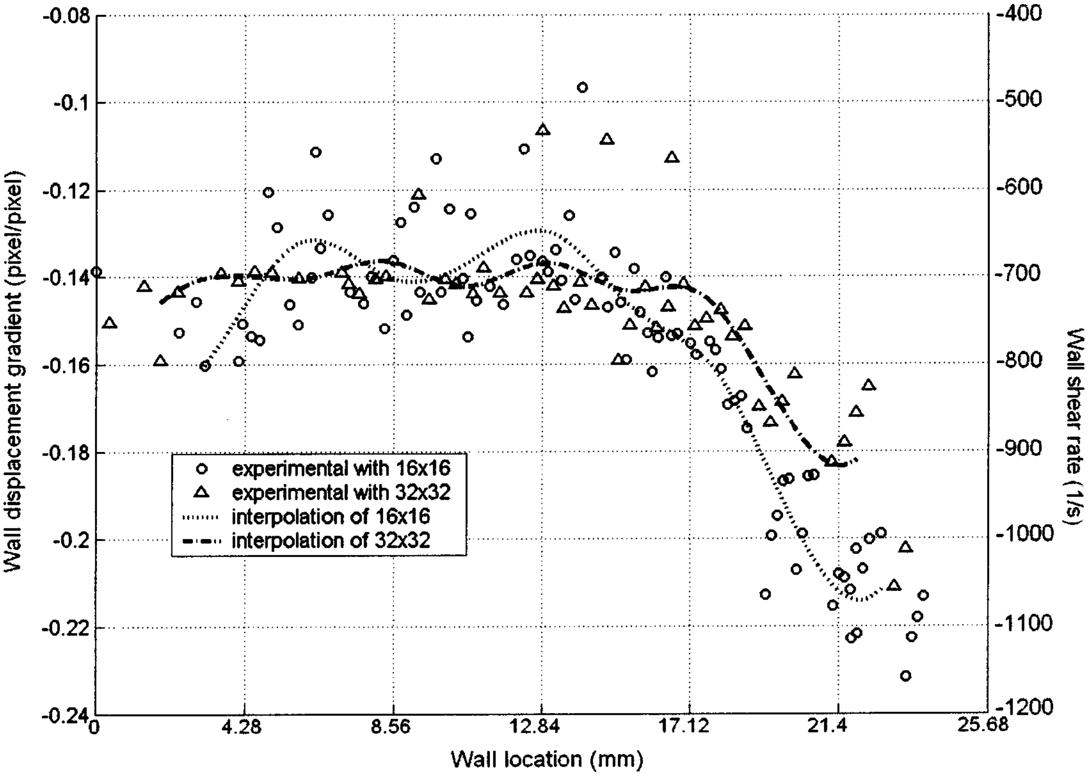

Fig. 9 The wall displacement and wall shear-rate of the bottom wall (curved surface) of the main chamber obtained by two different interrogation window sizes.

extrapolate wall shear-rate from the velocity vector field obtained by PIV, several additional issues were considered, such as the accuracy of vector location and the wall shear-rate interpolation algorithm.

The simplicity of the techniques employed provides the flexibility to be used with different surface geometries. In addition, wall shear-rate estimates can be obtained for a large number of locations (e.g. the entire artificial heart) rapidly. The flexibility and relative speed of acquiring these measurements allow them to be included as part of a design process.

The experimental results indicate that more accurate shear-rate estimates may require the use of higher magnification and more specialized techniques. Preliminary work in this direction may be found in Hochareon [29]. While the shear rates obtained using this technique are detailed in a subsequent paper, the results suggest that shear rates (approximately $200\ \mathrm{s}^{-1}$) along the bottom of the chamber may provide an area for thrombogenesis in a similar region where a loosely attached clot was found in vivo.

Acknowledgements

This research was supported through the NIH on Grant HL60276.

References

[1] DeVries, W. C., Anderson, J. L., Joyce, L. D., Anderson, F. L., Hammond, E. H., Jarvik, R. K., and Kolff, W. J., 1984, ''Clinical Use of the Total Artificial Heart,'' N. Engl. J. Med., **310**, pp. 273–278.

[2] Bachmann, C., Hugo, G., Rosenberg, G., Deutsch, S., Fontaine, A., and Tarbell, J. M., 2000, ''Fluid Dynamics of a Pediatric Ventricular Assist Device,'' Artif. Organs, **24**, pp. 362–372.

[3] Magovern, J. A., Pennock, J. L., Campbell, D. B., Pae, Jr., W. E., Pierce, W. S., and Waldhausen, J. A., 1986, ''Bridge to Heart Transplantation: The Penn State Experience,'' J. Heart Transplant, **5**, pp. 196–202.

[4] Orvim, U., Barstad, R. M., Orning, L., Petersen, L. B., Ezban, M., Hedner, U., and Sakariassen, K. S., 1997, ''Antithrombotic Efficacy of Inactivated Active Site Recombinant Factor VIIa is Shear Dependent in Human Blood,'' Arterioscler. Thromb. Vasc. Biol., **17**, pp. 3049–3056.

[5] Holme, P. A., Orvim, U., Hamers, M. J., Solum, N. O., Brosstad, F. R., Barstad, R. M., and Sakariassen, K. S., 1997, ''Shear-Induced Platelet Activation and Platelet Microparticle Formation at Blood Flow Conditions as in Arteries with a Severe Stenosis,'' Arterioscler. Thromb. Vasc. Biol., **17**, pp. 646–653.

[6] Badimon, L., Badimon, J. J., Galvez, A., Chesebro, J. H., and Fuster, V., 1986, ''Influence of Arterial Damage and Wall Shear Rate on Platelet Deposition. Ex Vivo Study in a Swine Model,'' Arteriosclerosis (Dallas), **6**, pp. 312–320.

[7] Phillips, W. M., Brighton, J. A., and Pierce, W. S., 1972, ''Artificial Heart Evaluation Using Flow Visualization Techniques,'' Trans. ASAIO, **18**, pp. 194–201.

[8] Mann, K. A., 1985, ''Fluid Dynamic Analysis of Newtonian and Non-Newtonian Fluids in a Penn State Ventricular Assist Device,'' M.S. thesis, The Pennsylvania State University, University Park, PA.

[9] Affeld, A., 1979, ''The State of the Art of the Berlin Total Artificial Heart-Technical Aspects,'' Assisted Circulation, F. Unger, ed., Springer-Verlag, New York, pp. 307–333.

[10] Tarbell, J. M., Gunshinan, J. P., Geselowitz, D. B., Rosenberg, G., Shung, K. K., and Pierce, W. S., 1986, ''Pulsed Ultrasonic Doppler Velocity Measurements Inside a Left Ventricular Assist Device,'' ASME J. Biomech. Eng., **108**, pp. 232–238.

[11] Phillips, W. M., Furkay, S. S., and Pierce, W. S., 1979, ''Laser Doppler Anemometer Studies in Unsteady Ventricular Flows,'' Trans. ASAIO, **25**, pp. 56–60.

[12] Baldwin, J. T., Tarbell, J. M., Deutsch, S., Geselowitz, D. B., and Rosenberg, G., 1988, ''Hot-Film Wall Shear Probe Measurements Inside a Ventricular Assist Device,'' ASME J. Biomech. Eng., **110**, pp. 326–333.

[13] Baldwin, J. T., 1987, ''Wall Shear Stress Measurements in the Penn State Ventricular Assist Device Using Hot-Film Anemometry,'' M.S. thesis, The Pennsylvania State University, University Park, PA.

[14] Baldwin, J. T., Deutsch, S., Geselowitz, D. B., and Tarbell, J. M., 1994, ''LDA Measurements of Mean Velocity and Reynolds Stress Fields within an Artificial Heart Ventricle,'' ASME J. Biomech. Eng., **116**, pp. 190–200.

[15] Kertzscher, U., Debaene, P., and Affeld, K., 2001, ''New Method to Visualize and to Measure the Wall Shear Rate in Blood Pumps,'' 4th International Symposium on Particle Image Velocimetry, Gottingen, Germany.

[16] Raffel, M., Willert, C. E., and Kompenhans, J., 1998, Particle Image Velocimetry: A Practical Guide. Springer-Verlag, Berlin.

[17] Keane, R. D., and Adrian, R. J., 1992, ''Theory of Cross-Correlation Analysis of PIV Images,'' Appl. Sci. Res., **49**, pp. 191–215.

[18] Adrian, R. J., 1991, ''Particle-Imaging Techniques for Experimental Fluid-Mechanics,'' Annu. Rev. Fluid Mech., **23**, pp. 261–304.

[19] Crowe, C. T., Sommerfeld, M., and Tsuji, Y., 1998, Multiphase flows with droplets and particles. CRC Press, Boca Raton, FL.

[20] Scarano, F., 2002, ''Iterative Image Deformation Methods in PIV,'' Meas. Sci. Technol., **13**, pp. R1–R19.

[21] Scarano, F., and Riethmuller, M. L., 1999, ''Iterative Multigrid Approach in PIV Image Processing with Discrete Window Offset,'' Exp. Fluids, **26**, pp. 513–523.

[22] Roth, G. I., and Katz, J., 2001, ''Five Techniques for Increasing the Speed and Accuracy of PIV Interrogation,'' Meas. Sci. Technol., **12**, pp. 238–245.

[23] Hart, D. P., 2000, ''PIV Error Correction,'' Exp. Fluids, **29**, pp. 13–22.

[24] Cox, R. G., and Mason, S. G., 1971, ''Suspended Particles in Fluid Flow through Tubes,'' Annu. Rev. Fluid Mech., **3**, pp. 291–318.

[25] Forliti, D. J., Strykowski, P. J., and Debatin, K., 2000, ''Bias and Precision Errors of Digital Particle Image Velocimetry,'' Exp. Fluids, **28**, pp. 436–447.

[26] Huang, H. T., Fiedler, H. E., and Wang, J. J., 1993, ''Limitation and Improvement of PIV-1. Limitation of Conventional Techniques Due to Deformation of Particle Image Patterns,'' Exp. Fluids, **15**, pp. 168–174.

[27] Abrahamson, S., and Lonnes, S., 1995, ''Uncertainty in Calculating Vorticity from 2D Velocity Fields Using Circulation and Least-Squares Approaches,'' Exp. Fluids, **20**, pp. 10–20.

[28] Lourenco, L., and Krothapalli, A., 1995, ''On the Accuracy of Velocity and Vorticity Measurements with PIV,'' Exp. Fluids, **18**, pp. 421–428.

[29] Hochareon, P., 2003, ''Development of Particle Imaging Velocimetry (PIV) for Wall Shear Stress Estimation within a 50cc Penn State Artificial Heart Ventricular Chamber,'' PhD thesis, The Pennsylvania State University, University Park, PA.

[30] Wernet, M. P., 2000, ''Application of DPIV to study both steady state and transient turbomachinery flows,'' Opt. Laser Technol., **32**, pp. 497–525.

[31] Christensen, K. T., and Adrian, R. J., 2002, ''The velocity and acceleration signatures of small-scale vortices in turbulent channel flow,'' J. Turbulence, **3**, 023.

[32] Kiesow, R. O., and Plesniak, M. W., 2003, ''Near-wall physics of a shear-driven three-dimensional turbulent boundary layer with varying crossflow,'' J. Fluid Mech., **484**, pp. 1–39.

[33] Hart, D. P., 1998, ''High-Speed PIV Analysis Using Compressed Image Correlation,'' ASME J. Fluids Eng., **120**, pp. 463–470.

[34] Hart, D. P., 1999, ''Super-Resolution PIV by Recursive Local-Correlation,'' J. Visualization, **10**, pp. 1–10.

[35] Hart, D. P., 1998, ''The Elimination of Correlation Errors in PIV Processing,'' 9th International Symposium on Applications of Laser Techniques to Fluid Mechanics, Lisbon, Portugal, 1998.

[36] Westerweel, J., 1994, ''Efficient Detection of Spurious Vectors in Particle Image Velocimetry Data,'' Exp. Fluids, **16**, pp. 236–247.

[37] Fikse, T. H., Rosenberg, G., Snyder, A. J., Landis, D. L., Hanson, K. L., Kern, S. E., Geselowitz, D. B., and Pierce, W. S., 1984, ''Development and Verification of EVAD/Mock Loop System Model,'' Frontiers of Engineering and Computing in Health Care-1984, Proceedings, Sixth Annual Conference-IEEE Engineering in Medicine and Biology Society, Los Angeles, CA.

[38] Hochareon, P., Manning, K. B., Fontaine, A. A., Deutsch, S., and Tarbell, J. M., 2002, ''Development of High Resolution Particle Image Velocimetry (PIV) for Use in Artificial Heart Research,'' Proc. Second Joint Meeting of the IEEE-EMBS and BMES, Houston, TX, p. 276.